LETTER

https://doi.org/10.1038/s41586-018-0276-y

North Pacific freshwater events linked to changes in glacial ocean circulation

E. Maier[1]*, X. Zhang[1]*, A. Abelmann[1], R. Gersonde[1], S. Mulitza[2], M. Werner[1], M. Méheust[1], J. Ren[1], B. Chapligin[3], H. Meyer[3], R. Stein[1], R. Tiedemann[1] & G. Lohmann[1]

There is compelling evidence that episodic deposition of large volumes of freshwater into the oceans strongly influenced global ocean circulation and climate variability during glacial periods[1,2]. In the North Atlantic region, episodes of massive freshwater discharge to the North Atlantic Ocean were related to distinct cold periods known as Heinrich Stadials[1–3]. By contrast, the freshwater history of the North Pacific region remains unclear, giving rise to persistent debates about the existence and possible magnitude of climate links between the North Pacific and North Atlantic oceans during Heinrich Stadials[4,5]. Here we find that there was a strong connection between changes in North Atlantic circulation during Heinrich Stadials and injections of freshwater from the North American Cordilleran Ice Sheet to the northeastern North Pacific. Our record of diatom $\delta^{18}O$ (a measure of the ratio of the stable oxygen isotopes ^{18}O and ^{16}O) over the past 50,000 years shows a decrease in surface seawater $\delta^{18}O$ of two to three per thousand, corresponding to a decline in salinity of roughly two to four practical salinity units. This coincided with enhanced deposition of ice-rafted debris and a slight cooling of the sea surface in the northeastern North Pacific during Heinrich Stadials 1 and 4, but not during Heinrich Stadial 3. Furthermore, results from our isotope-enabled model[6] suggest that warming of the eastern Equatorial Pacific during Heinrich Stadials was crucial for transmitting the North Atlantic signal to the northeastern North Pacific, where the associated subsurface warming resulted in a discernible freshwater discharge from the Cordilleran Ice Sheet during Heinrich Stadials 1 and 4. However, enhanced background cooling across the northern high latitudes during Heinrich Stadial 3—the coldest period in the past 50,000 years[7]—prevented subsurface warming of the northeastern North Pacific and thus increased freshwater discharge from the Cordilleran Ice Sheet. In combination, our results show that nonlinear ocean–atmosphere background interactions played a complex role in the dynamics linking the freshwater discharge responses of the North Atlantic and North Pacific during glacial periods.

During the last glacial period (roughly 115,000 to 12,000 years ago), large parts of the North American continent were covered by the North American Ice Sheet Complex, which comprised the Laurentide Ice Sheet (LIS) in the centre and east, and the smaller Cordilleran Ice Sheet (CIS) in the west (Fig. 1). The LIS was a source of major freshwater discharge events into the North Atlantic Ocean during Heinrich Stadials. It has been proposed that the resulting weakening of the Atlantic meridional overturning circulation (AMOC)[3,8] also influenced circulation in the North Pacific Ocean[5,9]. However, the dynamical connections between glacial ocean circulation changes and CIS dynamics remain elusive.

Because freshwater is a major modulator of ocean stratification and hence vertical mixing, reconstructions of North Pacific freshwater flux history help in elucidating the evolution of climate in the North Pacific. During the last glacial, the ice volume of the CIS was around 4–16 times larger than it is today[10], making it a major source of freshwater for the northeastern North Pacific. To date, however, palaeoclimate reconstructions have shown conflicting results with respect to freshwater flux from the CIS. Large deposits of ice-rafted debris (IRD) have been observed in a few coastal settings of the northeastern North Pacific during Heinrich Stadials, indicating episodic freshwater input from melting icebergs[11]. However, $\delta^{18}O$ records from planktic foraminifera ($\delta^{18}O_{pl.foram.}$) in the open northeastern North Pacific are not (unlike their North Atlantic counterparts) characterized by the anomalously light values that are indicative of freshwater input during Heinrich Stadials[12,13] (Fig. 2e). This discrepancy can potentially be attributed to the subsurface habitat of the studied foraminifera[12], highlighting the need for a more suitable proxy for recording surface-water isotope conditions in the North Pacific. Here we provide a roughly 50,000-year-long $\delta^{18}O$ record from the open northeastern North Pacific reconstructed from diatoms ($\delta^{18}O_{diat.}$), which are unicellular algae with siliceous shells that are bound to the surface-water layer. In combination with a water-isotope-enabled, fully coupled climate model[6], we are able to conduct a direct data–model comparison regarding $\delta^{18}O$ changes, allowing a fresh perspective on the dynamic link between the climate histories of the North Atlantic and North Pacific during Heinrich Stadials.

Our $\delta^{18}O_{diat.}$ record was obtained from kasten core SO202-27-6 (30 cm × 30 cm), recovered in the catchment area of the CIS (54.3° N, 149.6° W; water depth 2,919 m; Fig. 1). The record is characterized by two prominent $\delta^{18}O_{diat.}$ minima with transient decreases in $\delta^{18}O_{diat.}$ of around 2‰–3‰—one during late Marine Isotope Stage (MIS) 2 (ref. [12]), and one during MIS3 (Fig. 2b). The two minima are observed with similar magnitude in the reconstructed surface seawater $\delta^{18}O$ ($\delta^{18}O_{sw}$) (Fig. 2c), obtained after correcting the $\delta^{18}O_{diat.}$ record for global ice volume and temperature (see Methods). The age of the younger $\delta^{18}O_{sw}$ minimum is well constrained, and coincides with Heinrich Stadial 1. The older surface $\delta^{18}O_{sw}$ minimum can be aligned to Heinrich Stadial 4 (Methods).

The surface $\delta^{18}O_{sw}$ signal is influenced by several factors, including ocean advection and the input of meteoric water. In the glacial North Pacific region, the meteoric input can be attributed mainly to in situ precipitation and CIS meltwater. The latter can be ascribed to the melting of icebergs—that is, when the CIS had a marine grounding line—or to flooding events related to the drainage of (sub)glacial lakes. To simulate climate responses in the North Pacific during Heinrich Stadial 1, we conducted two types of hosing experiments under the conditions of the Last Glacial Maximum (LGM; ref. [14]) by imposing freshwater flux either into the North Atlantic alone (LGM_NA) or additionally into the North Pacific (LGM_NA + NP) (Methods and Extended Data Table 1). To represent $\delta^{18}O_{sw}$ changes caused by freshwater input to the North Atlantic and northeastern North Pacific, we used a uniform $\delta^{18}O$ value of −30‰ for both the LGM_NA and the LGM_NA + NP hosing components, corresponding to the average composition of the LIS (see Methods). This isotopic value enables us to quantify the smallest amount of freshwater needed to account for the reconstructed $\delta^{18}O$ variations in our record (Methods).

[1]Alfred Wegener Institute Helmholtz Centre for Polar and Marine Research, Bremerhaven, Germany. [2]MARUM—Center for Marine Environmental Sciences, University of Bremen, Bremen, Germany. [3]Alfred Wegener Institute Helmholtz Centre for Polar and Marine Research, Potsdam, Germany. *e-mail: edith.maier@awi.de; xu.zhang@awi.de

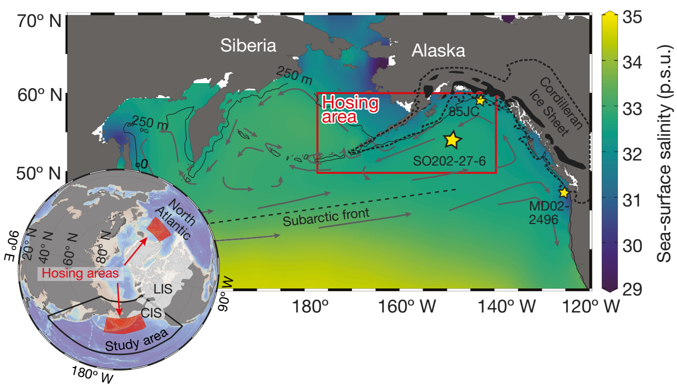

Fig. 1 | Study area. Inset, our study area in the North Pacific, and the areas in the North Atlantic and North Pacific that we chose for freshwater hosing in our palaeoclimate models. The shaded white areas represent the extents of the LIS and CIS during the LGM (see Extended Data Fig. 3). Main image, modern North Pacific sea-surface salinity[30] and the northeastern North Pacific hosing area (red rectangle). Arrows represent the modern surface water circulation. Also shown are the locations of cores SO202-27-6 (large yellow star), MD02-2496 and EW0408-85JC (small yellow stars); the modern extent of Cordilleran glaciers (black areas); and the extent of the CIS during the LGM (see Extended Data Fig. 3) (black dashed line). Northern Hemisphere and sea-surface-salinity maps were created using Ocean Data View (see Extended Data Fig. 3).

In LGM_NA, the subarctic northeastern North Pacific is characterized by an increase in surface $\delta^{18}O_{sw}$ (Fig. 3d) resulting from enhanced advection of (sub)tropical, $\delta^{18}O_{sw}$-enriched surface waters, which substantially outweighs the counteracting effects of the increased $\delta^{18}O_{sw}$-depleted precipitation (Extended Data Fig. 1a, b). This effect is related to the low glacial sea levels (which were about 120 m lower than at present)[15] and a closed Bering Strait, which prevented the inflow of fresh North Atlantic surface waters to the North Pacific during Heinrich Stadials 1–4 (ref. [16]). Therefore, a substantial freshwater flux (around 0.1 sverdrups, Sv) from the CIS into the North Pacific must be invoked in the model to explain the observed decrease in surface $\delta^{18}O_{sw}$ (Figs. 2c, 3i). Indeed, enhanced IRD abundances in glacial deposits until Heinrich Stadial 1 (Fig. 2a)—including pebble-to-cobble-sized dropstones in the intervals assigned to Heinrich Stadials 2 and 4 (Extended Data Fig. 2a)—suggest the existence of a marine-based CIS, that is, a CIS with a grounding line in the North Pacific, during most of the last glacial period. Furthermore, these enhanced IRD abundances indicate that the freshwater flux from melting icebergs reached the open northeastern North Pacific during Heinrich Stadials. Besides iceberg melting, flooding events from (sub)glacial lakes[17–19] could have provided additional freshwater (Methods).

In contrast to the $\delta^{18}O_{diat.}$ record, the $\delta^{18}O_{pl.foram.}$ record from the same open ocean core—derived from sinistral *Neogloboquadrina pachyderma* specimens—shows slightly elevated values during Heinrich Stadials 1 and 4 (Fig. 2e), indicating a local cooling and/or enrichment of $\delta^{18}O_{sw}$. Sinistral *N. pachyderma* are subsurface dwellers and respond to the depth of the pycnocline, which is at roughly 150 m at the study site (see Methods). In both hosing experiments, simulated subsurface $\delta^{18}O_{pl.foram.}$ appears to be in general agreement with observed changes in sinistral *N. pachyderma* $\delta^{18}O_{pl.foram.}$ values (Fig. 3e, j). This can probably be attributed to a coherent subsurface cooling in both experiments (Fig. 3b, g), given their contrasting responses in subsurface $\delta^{18}O_{sw}$—namely a depletion in LGM_NA+NP but enrichment in LGM_NA (Extended Data Fig. 1d, h). Like our open-ocean subsurface record, surface $\delta^{18}O_{sw}$ records reconstructed from the coastal northeastern North Pacific, based on $\delta^{18}O_{pl.foram.}$ data from *Globigerina bulloides*, do not show distinctly depleted $\delta^{18}O_{sw}$ values during times of elevated IRD deposition[13,20,21] (Fig. 4d, e, g). This finding could be related to the proximity of the coastal sites to the CIS margin, which resulted in only a small difference between the local background $\delta^{18}O_{sw}$ values and

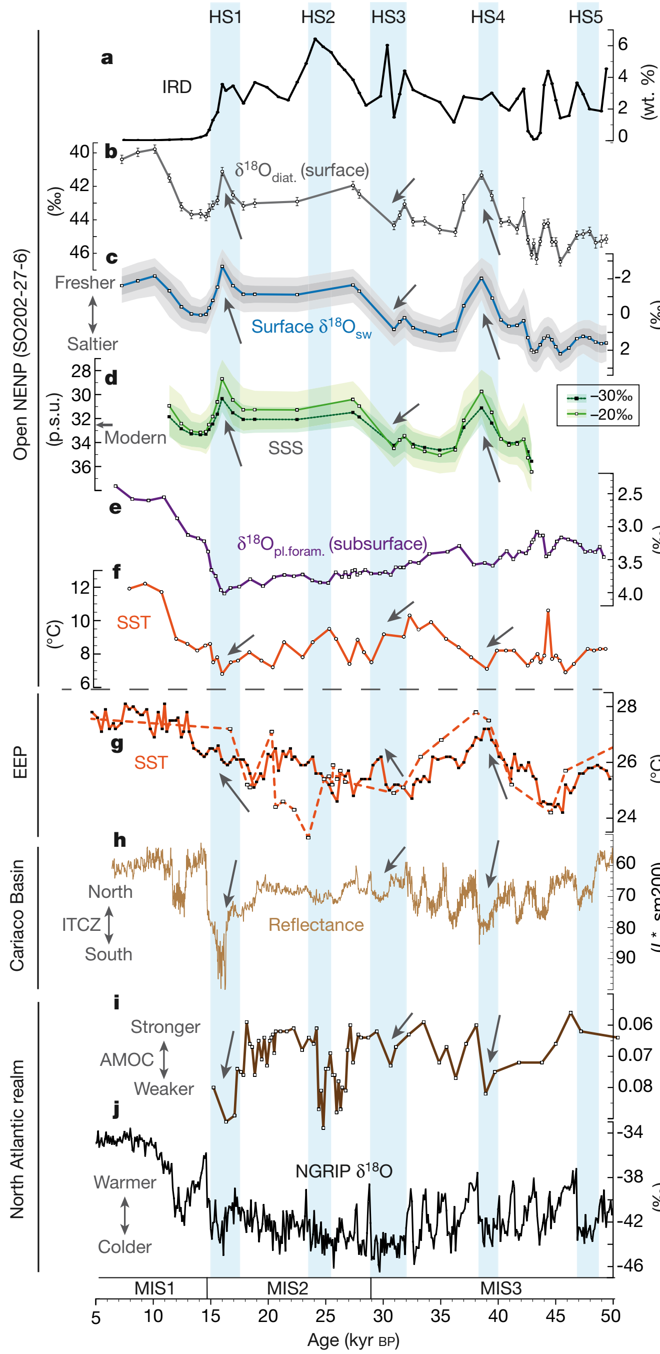

Fig. 2 | Proxy data from the North Pacific and North Atlantic (50 kyr to 5 kyr BP). a–f, Data from northeastern North Pacific core SO202-27-6 (in **b**, **e** and **f**, data for the past 25 kyr BP are from ref. [12]). **a**, Ice-rafted debris. **b**, $\delta^{18}O_{diat.}$ data; error bars show the errors of replicate analyses or the long-term reproducibility of standards (1σ). **c**, Surface $\delta^{18}O_{sw}$; dark grey and light grey envelopes show 68% and 95% confidence intervals, respectively. **d**, Sea-surface salinity calculated from surface $\delta^{18}O_{sw}$; green envelopes show 95% confidence intervals, assuming a CIS meltwater $\delta^{18}O$ of −20‰ (light green) or −30‰ (dark green). **e**, Subsurface $\delta^{18}O_{pl.foram.}$ data from sinistral *N. pachyderma*. **f**, Alkenone-based SSTs. **g**, Alkenone-based (solid line) and magnesium/calcium-based (dashed line) SSTs (from the eastern Equatorial Pacific, core MD02-2529; ref. [25]). **h**, Sediment total reflectance (from the Cariaco Basin; ref. [24]). L^*, lightness; sm200, 200-point running mean. **i**, $^{231}Pa/^{230}Th$ ratio (Ocean Drilling Program (ODP) site 1063; ref. [3]). **j**, NGRIP $\delta^{18}O$ record[7]. EEP, eastern Equatorial Pacific; HS, Heinrich Stadial; ITCZ, Intertropical Convergence Zone. Arrows indicate the direction of proxy changes during Heinrich Stadials 1, 3 and 4.

the CIS freshwater $\delta^{18}O$ value (ref. [20]). However, the surface $\delta^{18}O_{sw}$ at our site (today around −0.5‰; ref. [22]) differed substantially from the CIS freshwater $\delta^{18}O$, so our surface-confined $\delta^{18}O_{diat.}$ record probably

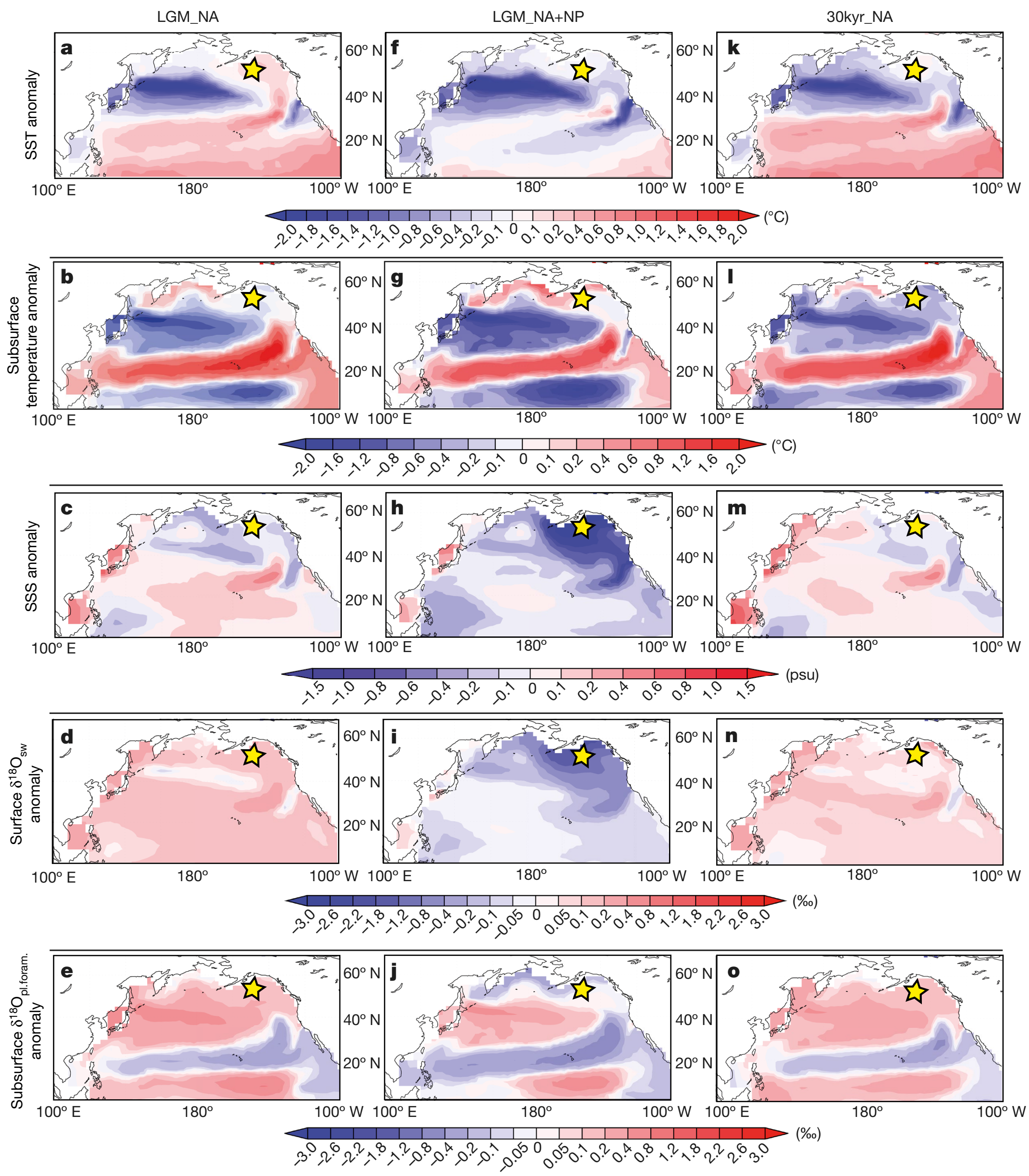

Fig. 3 | Results of freshwater hosing experiments LGM_NA, LGM_NA+NP and 30kyr_NA. Model results are presented as anomalies between the hosing simulations and the LGM state (see Methods). Left, results from LGM_NA. Middle, results from LGM_NA+NP. Right, results from 30kyr_NA. **a**, **f**, **k**, SST anomalies. **b**, **g**, **l**, Subsurface temperature anomalies (120–180 m depth). **c**, **h**, **m**, SSS anomalies. **d**, **i**, **n**, Surface $\delta^{18}O_{sw}$ anomalies. **e**, **j**, **o**, Subsurface $\delta^{18}O_{pl.foram.}$ anomalies (150 m). The yellow star marks the location of the studied core SO202-27-6.

follows the $\delta^{18}O_{sw}$ changes associated with freshwater discharges. Given assumed isotopic values of −20‰ to −30‰ for glacial Cordilleran ice (Methods), decreases of around 2‰–3‰ in surface $\delta^{18}O_{sw}$ correspond to decreases in sea-surface salinity (SSS) of around 2–4 practical salinity units (p.s.u.; Fig. 2d and Extended Data Fig. 3). Such decreases are consistent with our LGM_NA+NP results (which show a simulated decrease in SSS of around 2 p.s.u., and in surface $\delta^{18}O_{sw}$ of about 2‰; Fig. 3h, i). The influence of precipitation changes on SSS is probably minor, given that total precipitation changes by less than 5 mm per month in our LGM_NA+NP experiment, and that the simulated precipitation $\delta^{18}O$ values decrease only slightly (less than 1‰; Extended Data Fig. 1e, f).

The close temporal correlation of CIS freshwater events to Heinrich Stadials indicates a potential dynamic link of meltwater events between the North Atlantic and North Pacific. External forcing of Northern Hemisphere summer insolation is thought to have initially triggered LIS retreat during glacial terminations[23], and might also have driven CIS freshwater discharge during Heinrich Stadial 1 (ref. [12]). However, given that such insolation forcing was limited during Heinrich Stadial 4 (Extended Data Fig. 2g), alternative trigger mechanisms should be considered. We propose that the observed recurring CIS meltwater events can be attributed to a weakened AMOC, which leads to positive feedbacks in the northeastern North Pacific in the presence of a marine-based CIS, through interactions between low and high latitudes and between the ocean and the atmosphere.

In our LGM_NA experiment, the weakened AMOC reduces meridional heat transport to the northern high latitudes, resulting in a southward shift of the Intertropical Convergence Zone[24] (Fig. 2h, i) and increased (sub)surface temperatures in the eastern Equatorial Pacific[25,26] (Figs. 2g and 3a, b). As a consequence, rainfall in the western Equatorial Pacific decreased, ultimately strengthening the Aleutian Low pressure system[27] (see Methods and Extended Data Fig. 4a). This led to increased poleward transport of (sub)tropical waters under the southeastern flank of the enhanced Aleutian

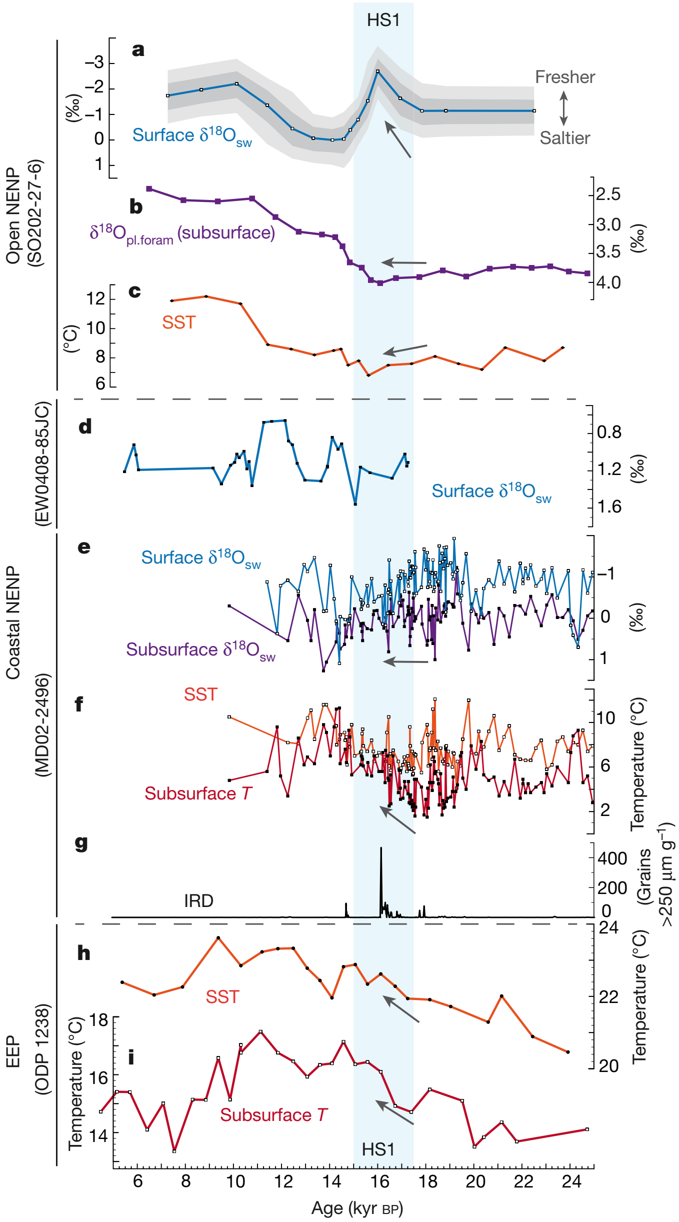

Fig. 4 | Proxy data from the eastern Equatorial Pacific (EEP) and northeastern North Pacific (NENP). **a–c**, Open-ocean NENP (core SO202-27-6). **a**, Surface $\delta^{18}O_{sw}$, with dark grey and light grey envelopes indicating the 68% and 95% confidence intervals, respectively, including age and analytical uncertainties. **b**, Subsurface sinistral *N. pachyderma* $\delta^{18}O_{pl.foram.}$ (ref. [12]). **c**, Alkenone-based SSTs[12]. **d–f**, Coastal NENP. **d**, Surface $\delta^{18}O_{sw}$ (from core EW0408-85JC; ref. [21]). **e**, (Sub)surface $\delta^{18}O_{sw}$ (ref. [20]). **f**, (Sub)surface temperature (*T*; ref. [20]) from core MD02-2496. **g**, IRD[11] from core MD02-2496. **h**, **i**, EEP. **h**, SSTs (magnesium/calcium-based, from *Globigerinoides sacculifer*) from ODP site 1238 (ref. [25]). **i**, Subsurface temperature (magnesium/calcium-based, from *Neogloboquadrina dutertrei*) from ODP site 1238 (ref. [25]). Arrows indicate the direction of proxy changes during Heinrich Stadials 1, 3 and 4.

Low, causing subsurface warming along the coastal northeastern North Pacific (Figs. 3b and 4f). The subsurface warming resulted in increased basal melting/calving of the marine-based CIS, leading to freshwater input to the northeastern North Pacific—a similar feedback to that proposed for glacial discharge events from the LIS[28] and the Antarctic ice sheets[29]. Our LGM_NA+NP results show weakened vertical mixing in response to surface water freshening, causing surface cooling and subsurface warming (Figs. 2d, f and 3f–h), which act as a local positive feedback mechanism to further accelerate the release of CIS meltwater.

This proposed mechanism links climate fluctuations observed in the North Atlantic, eastern Equatorial Pacific and northeastern North Pacific during Heinrich Stadials 1 and 4. During Heinrich Stadial 3, however, the increases in SSS and surface $\delta^{18}O_{sw}$ at our site do not indicate increased CIS meltwater discharge (Fig. 2c, d). A robust data evaluation for Heinrich Stadial 3 is precluded by the absence of $\delta^{18}O_{diat.}$ data for the time of the maximum Heinrich Stadial 3 IRD abundance, as a consequence of the low biogenic opal content of less than 5% in the sediments (as for the sediments corresponding to Heinrich Stadial 2). Nevertheless, to test the dynamic link between the North Atlantic and North Pacific during this stadial, we performed an additional North Atlantic hosing experiment under conditions of 30,000 years ago (30kyr_NA; Extended Data Table 1). As for LGM_NA, 30kyr_NA shows warming in the eastern Equatorial Pacific and an increased Aleutian Low (Fig. 3k, l and Extended Data Fig. 4b), indicating that the first part of the dynamic link—that is, the teleconnection between the North Atlantic and eastern Equatorial Pacific—also works during Heinrich Stadial 3. However, the simulated (sub)surface cooling, surface $\delta^{18}O_{sw}$ enrichment and SSS increase at our site (Fig. 3k–n), which match our proxy data (Fig. 2c, d, f), indicate that the warm and salty (sub)tropical water masses cooled down before reaching the coastal northeastern North Pacific. Given that Heinrich Stadial 3 was the coldest period of the past 50,000 years in the northern high latitudes[7], it seems that the enhanced Northern Hemisphere cooling under 30-kyr orbital forcing supersedes the warming effect from the subtropics, preventing massive CIS meltwater events during Heinrich Stadial 3 (Methods). Therefore, background cooling in the northern high latitudes acts as a critical negative feedback on the collapse of marine-based CIS ice, modulating the dynamic link between the North Atlantic and North Pacific during Heinrich Stadials.

The results of our data–model comparison provide compelling evidence that, during North Atlantic cold stadials characterizing the past 50,000 years, perturbations to the AMOC could have been teleconnected to the northeastern North Pacific region, triggering freshwater discharge events via interactions between low and high latitudes and between oceans and the atmosphere. Until now, such North Pacific freshwater input events have not been considered as standard forcing components in glacial climate simulations; the incorporation of this freshwater forcing scenario provides a new basis for research that could reconcile the discrepancies within proxy data regarding the responses of North Pacific ocean circulation to AMOC changes. For example, because of the limitations of age-model constraints in the North Pacific (related to poor knowledge of palaeoreservoir ages), it is difficult to assess the lead–lag relationship of North Pacific meltwater events with changes in the AMOC using proxy data. However, on the basis of a North Pacific hosing experiment with LGM boundary conditions (LGM_NP; Extended Data Table 1), it seems that North Pacific meltwater discharge alone leads to subsurface cooling in the North Atlantic (Extended Data Fig. 5c), acting as an unlikely trigger of ice-surging events in the North Atlantic[28] and related AMOC changes (see Methods). Given that glacial meltwater events are closely associated with ice-sheet dynamics, climate models that incorporate interactive ice-sheet dynamics together with high-resolution proxy records from the open northeastern North Pacific are highly desirable to further assess the proposed dynamic linkages between the North Atlantic and North Pacific, as well as local feedbacks within the North Pacific.

Online content

Any Methods, including any statements of data availability and Nature Research reporting summaries, along with any additional references and Source Data files, are available in the online version of the paper at https://doi.org/10.1038/s41586-018-0276-y.

Received: 26 July 2017; Accepted: 14 May 2018;
Published online 11 July 2018.

1. Maslin, M. A., Shackleton, N. J. & Pflaumann, U. Surface water temperature, salinity, and density changes in the northeast Atlantic during the last 45,000 years: Heinrich events, deep water formation, and climatic rebounds. *Paleoceanography* **10**, 527–544 (1995).

2. Kageyama, M. et al. Climatic impacts of fresh water hosing under Last Glacial Maximum conditions: a multi-model study. *Clim. Past* **9**, 935–953 (2013).
3. Böhm, E. et al. Strong and deep Atlantic meridional overturning circulation during the last glacial cycle. *Nature* **517**, 73–76 (2015).
4. Praetorius, S. & Mix, A. Synchronisation of North Pacific and Greenland climates preceded abrupt deglacial warming. *Science* **345**, 444–448 (2014).
5. Menviel, L., England, M. H., Meissner, K. J., Mouchet, A. & Yu, J. Atlantic-Pacific seesaw and its role in outgassing CO_2 during Heinrich events. *Paleoceanography* **29**, 58–70 (2014).
6. Werner, M. et al. Glacial-interglacial changes in $H_2{}^{18}O$, HDO and deuterium excess—results from the fully coupled ECHAM5/MPI-OM Earth system model. *Geosci. Model Dev*. **9**, 647–670 (2016).
7. North Greenland Ice Core Project members. High-resolution record of Northern Hemisphere climate extending into the last interglacial period. *Nature* **431**, 147–151 (2004).
8. Henry, L. G. et al. North Atlantic ocean circulation and abrupt climate changes during the last glaciation. *Science* **353**, 470–474 (2016).
9. Chikamoto, M. O. et al. Variability in North Pacific intermediate and deep water ventilation during Heinrich events in two coupled climate models. *Deep Sea Res. Part II Top. Stud. Oceanogr*. **61–64**, 114–126 (2012).
10. Seguinot, J., Rogozhina, I., Stroeven, A. P., Margold, M. & Kleman, J. Numerical simulations of the Cordilleran ice sheet through the last glacial cycle. *Cryosphere Discuss*. **9**, 4147–4203 (2015).
11. Hendy, I. L. & Cosma, T. Vulnerability of the Cordilleran Ice Sheet to iceberg calving during late Quaternary rapid climate change events. *Paleoceanography* **23**, PA2101 (2008).
12. Maier, E. et al. Deglacial subarctic Pacific surface water hydrography and nutrient dynamics and links to North Atlantic climate variability and atmospheric CO_2. *Paleoceanography* **30**, 949–968 (2015).
13. Gebhardt, H. et al. Paleonutrient and productivity records from the subarctic North Pacific for Pleistocene glacial terminations I to V. *Paleoceanography* **23**, PA4212 (2008).
14. Zhang, X., Lohmann, G., Knorr, G. & Xu, X. Different ocean states and transient characteristics in Last Glacial Maximum simulations and implications for deglaciation. *Clim. Past* **9**, 2319–2333 (2013).
15. Siddall, M. et al. Sea-level fluctuations during the last glacial cycle. *Nature* **423**, 853–858 (2003).
16. Hu, A. et al. Influence of Bering Strait flow and North Atlantic circulation on glacial sea-level changes. *Nat. Geosci*. **3**, 118–121 (2010).
17. Wiedmer, M., Montgomery, D. R., Gillespie, A. R. & Greenberg, H. Late Quaternary megafloods from Glacial Lake Atna, Southcentral Alaska, U.S.A. *Quat. Res*. **73**, 413–424 (2010).
18. Benito, G. & O'Connor, J. E. Number and size of last-glacial Missoula floods in the Columbia River valley between the Pasco Basin, Washington, and Portland, Oregon. *Geol. Soc. Am. Bull*. **115**, 624–638 (2003).
19. Livingstone, S. J., Clark, C. D. & Tarasov, L. Modelling North American palaeo-subglacial lakes and their meltwater drainage pathways. *Earth Planet. Sci. Lett*. **375**, 13–33 (2013).
20. Taylor, M. A., Hendy, I. L. & Pak, D. K. Deglacial ocean warming and marine margin retreat of the Cordilleran Ice Sheet. *Earth Planet. Sci. Lett*. **403**, 89–98 (2014).
21. Praetorius, S. et al. North Pacific deglacial hypoxic events linked to abrupt climate warming. *Nature* **527**, 362–366 (2015).
22. Kipphut, G. W. Glacial meltwater input to the Alaska Coastal Current: evidence from oxygen isotope measurements. *J. Geophys. Res*. **95**, 5177–5181 (1990).
23. Cheng, H. et al. Ice age terminations. *Science* **326**, 248–252 (2009).
24. Deplazes, G. et al. Links between tropical rainfall and North Atlantic climate during the last glacial period. *Nat. Geosci*. **6**, 213–217 (2013).
25. Martínez-Botí, M. A. et al. Boron isotope evidence for oceanic carbon dioxide leakage during the last deglaciation. *Nature* **518**, 219–222 (2015).
26. Leduc, G. et al. Moisture transport across Central America as a positive feedback on abrupt climatic changes. *Nature* **445**, 908–911 (2007).
27. Okumura, Y. M., Deser, C., Hu, A., Timmermann, A. & Xie, S.-P. North Pacific climate response to freshwater forcing in the subarctic North Atlantic: oceanic and atmospheric pathways. *J. Clim*. **22**, 1424–1445 (2009).
28. Marcott, S. A. et al. Ice-shelf collapse from subsurface warming as a trigger for Heinrich Events. *Proc. Natl Acad. Sci. USA* **108**, 13415–13419 (2011).
29. Weber, M. E. et al. Millennial-scale variability in Antarctic ice-sheet discharge during the last deglaciation. *Nature* **510**, 134–138 (2014).
30. Antonov, J. I. et al. *World Ocean Atlas 2009, Vol. 2: Salinity*. (NOAA Atlas NESDIS 69, US Gov. Print. Off., Washington DC, 2010).

Acknowledgements This work was largely part of the Innovative NOrth Pacific EXperiment (INOPEX), funded by the Bundesministerium für Bildung und Forschung. We also acknowledge funding by the Helmholtz Postdoc program (PD-301; to X.Z.), as well as Helmholtz funding through the Polar Regions and Coasts in the Changing Earth System (PACES) program of the Alfred Wegener Institute. Funding from the Qingdao National Laboratory for Marine Science and Technology (QNLM201703) is also acknowledged. We thank U. Böttjer, B. Glückselig and R. Cordelair for the thorough purification of diatom samples for isotope analyses; M. Warnkross for picking planktic foraminifera for stable-isotope analysis and radiocarbon dating; S. Steph and A. Mackensen for performing the foraminiferal oxygen-isotope analysis; and G. Knorr for helpful discussions.

Reviewer information *Nature* thanks S. Dee, A. Hu, K. Thirumalai and the other anonymous reviewer(s) for their contribution to the peer review of this work.

Author contributions E.M. and X.Z. designed the study and wrote the manuscript with contributions from A.A., R.G. and G.L. E.M. performed the diatom isotope measurements with support from B.C. and H.M. X.Z. designed the model experiments and performed simulations with support from M.W. and G.L. E.M. constructed the age model and S.M. carried out the proxy uncertainty modelling. E.M. performed the contamination analysis of diatom samples. M.M. and R.S. contributed alkenone-based sea-surface temperatures (SSTs), and J.R. the diatom composition of the isotope samples. All authors contributed to the final version of the manuscript.

Competing interests The authors declare no competing interests.

Additional information
Extended data is available for this paper at https://doi.org/10.1038/s41586-018-0276-y.
Reprints and permissions information is available at http://www.nature.com/reprints.
Correspondence and requests for materials should be addressed to E.M. or X.Z.
Publisher's note: Springer Nature remains neutral with regard to jurisdictional claims in published maps and institutional affiliations.

METHODS

Chronology. The chronology of core SO202-27-6 is based on 12 planktic ^{14}C ages, in combination with 15 additional age control points. The planktic foraminifera for planktic ^{14}C ages were picked from the 125–250-μm fraction and dated by accelerator mass spectrometry (AMS) at the National Ocean Science AMS facility (NOSAMS) at Woods Hole Oceanographic Institution (Extended Data Table 2). The 15 additional age control points, in between the planktic ^{14}C ages and below 243.5 cm, were obtained through two different approaches. First, in the upper-core section (0–91 cm), the five additional age control points (LS-1 to LS-5) correspond to the calibrated ages determined in ref. [12], which are ^{14}C plateau boundaries determined via proxy correlation to the high-resolution ^{14}C record of core MD02-2489 (ref. [12]). Second, the ten age control points in the lower part of the core (91–289 cm; NG-1 to NG-10) were determined by visual correlation between iron intensity and the NGRIP dust record[31] (Extended Data Table 2; Extended Data Fig. 2), assuming in-phase behaviour between both parameters. This assumption is reasonable because of the in-phase relationship between NGRIP dust and subarctic Pacific eolian dust[32], and between eolian dust and the iron intensity of northwestern North Pacific core SO202-07-6, over the last glacial–interglacial transition (Extended Data Fig. 6). The correlation between iron intensity and NGRIP dust record results in overall in-phase behaviour between increased calcium concentrations in the subarctic northeastern North Pacific and warm periods in the North Atlantic region, consistent with previous MIS3 age models from the northeastern North Pacific[33,34].

We used the R script BACON (ref. [35]) version 2.2 and the Marine13 calibration curve[36] to model down-core calendar age uncertainty. For the upper section of core SO202-27-6 (0–91 cm), we applied additional local reservoir ages (ΔR) of 40 ± 173 years (1σ) and 150 ± 185 years (1σ), consistent with the reservoir ages determined for nearby core MD02-2489 (ref. [37]), which was correlated to the upper part of core SO202-27-6 (0–91 cm) via proxy data[12]. For the lower-core section (91–289 cm) we applied a local reservoir age (ΔR) of 710 ± 202 years (1σ), as determined for ^{14}C-plateau IV for core MD02-2489 (ref. [37]), because no information is available on local reservoir ages and reservoir age changes during MIS3. Down-core calendar age distributions were modelled using BACON's default settings and a Student's t distribution (shape parameter t.a. = 20, scale parameter t.b. = 21) (Extended Data Fig. 7). From 10,000 age–depth realizations generated with BACON, we calculated the median age and the 95% confidence intervals at 1-cm resolution.

X-ray fluorescence measurements. The relative elemental compositions (in counts per second; c.p.s.) of core SO202-27-6 and core SO202-07-6 were measured at 1-cm resolution using an Avaatech X-ray fluorescence (XRF) core scanner located at the Alfred Wegener Institute, Bremerhaven, Germany. The elements iron and calcium used here for core chronology were obtained from scans performed at 1 mA, with a tube voltage of 10 kV and a counting time of 30 seconds.

Diatom samples for oxygen-isotope analysis. Diatom valves for oxygen-isotope analysis (91–289 cm) were extracted from bulk sediment samples obtained every 5 cm (2-cm-thick slices; 225 cm^3) from kasten core SO202-27-6. Diatom samples (100–125-μm fraction) were purified as in refs [12,38]. Briefly, bulk samples were liberated from carbonates and non-diatom silicates using a combination of physical and chemical treatments, including sonication and heavy liquid separation. Diatom assemblages were determined from microscopic slides, prepared before the sonication procedure, following the diatom taxonomy of refs [39,40]. Purified diatom samples were dominated by *Coscinodiscus* species (99.7 ± 1.2%), with a large contribution of *C. marginatus* (92.7 ± 9.6%) and a minor contribution of *C. oculus-iridis* (7.0 ± 9.5%) (Extended Data Fig. 8a). We checked the purified diatom samples for non-biogenic silicate contamination using energy-dispersive X-ray spectrometry (EDS) on subsamples of all purified diatom samples, and checked the EDS results by additional measurements using inductively coupled plasma optical emission spectrometry on six diatom samples (see also refs [12,38]). Aluminium oxide was used as a tracer for non-biogenic silicates, and mass balance corrections were applied[41], using two different $\delta^{18}O$ values (+2‰ and +30.00‰) for the contamination, corresponding to the isotopic range of non-biogenic silicates[42,43]. Contamination of all diatom samples from the last glacial period is less than 4%, except in the case of three samples from early MIS2 (Extended Data Fig. 8b), indicating a high purity of diatom samples. Mass-balance-corrected isotopic curves still show pronounced $\delta^{18}O_{diat.}$ minima during Heinrich Stadials 1 and 4 (Extended Data Fig. 8c), showing that the $\delta^{18}O_{diat.}$ minima are not the result of silicate contamination.

Diatom oxygen-isotope measurements. We used about 1.5–2.0 mg of purified material from SO202-27-6 diatom samples (91–289 cm) in order to measure the $\delta^{18}O_{diat.}$ composition using laser fluorination and a PDZ Europa 2020 mass spectrometer[44]. Values are reported in the common δ notation versus Vienna Standard Mean Ocean Water (V-SMOW), using the laboratory diatom standards PS1772-8$_{bsis}$ (marine) and BFC (lacustrine) calibrated against the International Atomic Energy Agency (IAEA) reference quartz standard National Bureau of Standards-28 (NBS-28). Analytical precision—determined by repeated analyses of PS1772-8$_{bsis}$ (two batches) and BFC over the periods when the samples were measured—was better than 0.25‰ (1σ), in line with published long-term reproducibility from this instrumentation[45]. (PS1772-8$_{bsis}$ (batch used for the interlaboratory comparison[45]): precision 43.49‰ ± 0.16‰, $n = 40$; PS1772-8$_{bsis}$ (subsequent batch): precision 44.15‰ ± 0.19‰, $n = 22$; BFC: precision 28.81‰ ± 0.24‰, $n = 10$.) Diatom samples were measured at least twice when enough purified material was available. Our record extends the $\delta^{18}O_{diat.}$ record (0–91 cm) published in ref. [12].

Foraminifera oxygen-isotope measurements. $\delta^{18}O$ measurements on sinistral *N. pachyderma* from core SO202-27-6 (91–289 cm) were carried out using a MAT 251 mass spectrometer directly coupled to an automated carbonate preparation device (Kiel I), and calibrated via the National Institute of Standards and Technology-19 (NIST-19) international standard to the Pee Dee Belemnite (PDB) scale. Sinistral *N. pachyderma* were picked from the 125–250 μm and the 315–400 μm fractions. All isotope values are given in δ notation versus Vienna-PDB (V-PDB). The precision of the measurements at 1σ, determined by repeated measurements of the internal Solnhofen limestone over a one-year period, was better than 0.08‰. This record extends the sinistral *N. pachyderma* $\delta^{18}O$ record (0–91 cm) of ref. [12].

IRD calculation. As an indicator of the abundance of IRD, we calculated the weight percentage of lithic and mineral grains of the >250-μm-to-2-mm fraction (medium-to-coarse sand), in accordance with previous IRD studies in the Gulf of Alaska[46,47]. We separated the lithic/mineral grains from the biogenic silicates by performing a heavy liquid separation (density = 2.2–2.3 g cm^{-3}) after organic and carbonate removal using hydrogen peroxide and hydrochloric acid. We regard the removal of carbonates as reasonable given that previous studies of sediments from the Gulf of Alaska showed that IRD in the open Gulf of Alaska generally consists of silicate minerals as well as siliciclastic, volcanic and metamorphic rock fragments[46]. We then sieved the heavy fraction at 250 μm and 2 mm (the light fraction was further cleaned for diatom isotope analysis) and normalized the weight of the >250-μm-to-2-mm fraction to the dry bulk sample weight. Dropstones (IRD larger than 2 mm) are not included in the calculation.

Alkenone-based SSTs. We determined alkenone-based SSTs from samples of core SO202-27-6 (91–289 cm) through gas chromatography (GC) and GC/mass spectrometry[48]. We determined the SSTs using the calibration of ref. [49], providing reasonable summer SST estimates for the (sub)arctic Pacific[48]. The standard error of the calibration is 1.5 °C. The total analytical error calculated from replicate analyses of an external alkenone standard (extracted from *Emiliana huxleyi* (EHUX) cultures with known growth temperatures) is less than 0.4 °C. Our SST record extends the record (0–91 cm) of ref. [12].

Calculation and error analysis of $\delta^{18}O_{sw}$ and SSS. To calculate local surface $\delta^{18}O_{sw}$, we generated 10,000 noisy Monte Carlo proxy realizations for the alkenone SSTs and $\delta^{18}O_{diat.}$ within the analytical uncertainty. We combined both proxy ensembles with BACON's age ensemble of similar size to obtain 10,000 possible time series for each proxy. All time series were interpolated to the median age obtained for the depth in which $\delta^{18}O_{diat.}$ was measured. The resulting SST and $\delta^{18}O_{diat.}$ time-series ensembles were used to calculate an ensemble of local surface $\delta^{18}O_{sw}$ with the following equation (ref. [50]):

$$\text{Local surface } \delta^{18}O_{SW} = \delta^{18}O_{diat} - 34 - \sqrt{122 - 5SST} - \text{mean}(\delta^{18}O_{SW})$$

with $\delta^{18}O_{diat.}$ being the measured diatom $\delta^{18}O$, SST being the temperature calculated from the alkenone-based SST record from the same core, and mean($\delta^{18}O_{sw}$) being the mean seawater $\delta^{18}O$. To account for global ice-volume-related changes in seawater $\delta^{18}O$, we corrected the resulting ensemble of local surface $\delta^{18}O_{sw}$ with a noisy ensemble of mean seawater $\delta^{18}O$ (from ref. [51]) before calculating the error envelopes. We consider the use of alkenone-based SSTs for the calculation of $\delta^{18}O_{sw}$ to be reasonable given that both coccolithophorids (which comprise the alkenone compounds) and diatoms of the genus *Coscinodiscus* (which make the $\delta^{18}O_{diat.}$ signal) (Extended Data Fig. 8a) contribute mainly to late-summer/autumn algal blooms in the subarctic Pacific region[48,52].

From the ensemble of ice-effect-corrected local surface $\delta^{18}O_{sw}$ records, we then calculated three different SSS records, assuming a linear regression between SSS and $\delta^{18}O_{sw}$ (Extended Data Fig. 3). We used a high-salinity endmember corresponding to simulated glacial subsurface waters at the study site (LGM control experiment at 150 m) ($\delta^{18}O$ = 0.71‰; salinity = 34.29 p.s.u.), which was introduced to the euphotic zone during autumn/winter mixing. For the low-salinity endmember (salinity = 0), we applied three freshwater sources with different $\delta^{18}O$ values, which correspond to: (1) the roughly average composition of modern CIS glaciers[22,53] (−20‰); (2) the roughly average composition of the LIS (−30‰)[54]; and (3) the average composition of modern precipitation at sea level in the Gulf of Alaska region (−8.6‰)[55]. We performed SSS estimations for only the time interval 43–11 kyr ago, which corresponds to the time period when the Bering strait was closed[16,56], as in our LGM control experiment[14].

Model description. We used a comprehensive, fully coupled atmosphere–ocean general circulation model (AO-GCM), namely COSMOS (ECHAM5-JSBACH-MPI-OM), for this study. The atmospheric component of this model

(ECHAM5)[57]—complemented by a land-surface component, JSBACH[58]—is used at 'T31' resolution (roughly 3.75°), with 19 vertical layers. The ocean model MPI-OM[59], which includes sea-ice dynamics that is formulated using viscous-plastic rheology[60], has a resolution of 'GR30' (roughly 3°) in the horizontal, with 40 uneven vertical layers. It has been used for a range of transient simulations, including a North Atlantic freshwater hosing simulation under preindustrial and LGM background states[14], and glacial millennial-scale climate variability[61,62]. To provide a direct comparison of water oxygen isotopes between proxy records and model outputs, we used the water-isotope-enabled version of COSMOS that has been used to simulate preindustrial and LGM distributions of $\delta^{18}O$, which are broadly consistent with observations[6].

Design of LGM_NA and LGM_NA+NP hosing experiments. To mimic the freshwater event from the CIS and explore its dynamic link to changes in the AMOC, we conducted two types of hosing experiment under LGM boundary conditions[14]. One was the typical North Atlantic hosing experiment, in which a constant freshwater flux of 0.15 Sv was imposed to the North Atlantic (40–55° N, 20–45° W) to mimic the freshwater discharge during Heinrich Stadial 1 (LGM_NA; Extended Data Table 1). The other hosing experiment also included a freshwater flux of 0.1 Sv to the northeastern North Pacific (50–60° N, 143–172° W) to represent rapid CIS retreat during Heinrich Stadial 1 (LGM_NA+NP). The isotopic values of the imposed freshwater in both cases were −30‰. This value is consistent with the average composition of the LIS[54], but is also specific to represent the assumed lower limit of isotopic value in the meltwater from the CIS. This set-up helped us to quantify the minimum amount of freshwater that is needed to reproduce the recorded magnitude of $\delta^{18}O_{sw}$ changes in the North Pacific, given that on the one hand meltwater from glacial lakes could be characterized by enriched $\delta^{18}O$ due to evaporative enrichment, and on the other hand such meltwater could be partly diluted before reaching our open-ocean study site. Both simulations were integrated for 800 model years, and the average of the last 100 years was used to represent the corresponding climatology. The reference climate state is the last 100-year average of the LGM simulation[6]. We note that the simulated $\delta^{18}O_{sw}$ at our core site does not differ substantially from that in the coastal regions, since our climate model (like many other climate models) is not able to explicitly resolve coastal hydrology.

Subsurface temperature and subsurface $\delta^{18}O_{sw}$ anomalies were taken for a water depth of 120–180 m. This corresponds to the water depth of the shelf area during the last glacial, considering the depth of the shelf area along the Pacific northwest coast today (250–300 m) and a maximum sea level lowstand of about −120 m during the last glacial[15]. The $\delta^{18}O_{pl.foram.}$ anomalies were taken from a water depth of 150 m, which corresponds to the depth of the pycnocline at the study site[63] and thus to the assumed habitat depth of subsurface sinistral *N. pachyderma* (ref. [64]). To calculate $\delta^{18}O_{pl.foram.}$ from simulated subsurface $\delta^{18}O_{sw}$ and simulated subsurface temperature, we used the equation for *N. pachyderma* from ref. [65].

Evaluation of freshwater sources. The main sources of freshwater to the northeastern North Pacific are freshwater from the CIS and precipitation. Besides iceberg melting, CIS meltwater related to flooding events from glacial lakes—located, for example, in Alaska[17] and at the southern lobe of the CIS[18]—and from subglacial lakes beneath the CIS[19] could have influenced our study site. Our SSS reconstruction (see above) shows that, when using the precipitation low-salinity endmember, SSS changes by about 10 p.s.u. during times of most depleted surface $\delta^{18}O_{sw}$, which would require a massive increase in precipitation and/or a massive decrease in precipitation $\delta^{18}O$. However, our LGM_NA results suggest only a small increase in precipitation of about 1–5 mm per day, with a small decrease in precipitation $\delta^{18}O$ to at most around 0.4‰, in the northeastern North Pacific during Heinrich Stadial 1 (Extended Data Fig. 1a, b). We therefore reject the idea that an increase in precipitation alone could be responsible for the surface $\delta^{18}O_{sw}$ minima. Moreover, precipitation contains a less negative $\delta^{18}O$ value compared with CIS freshwater, and therefore has a much lower effect on surface $\delta^{18}O_{sw}$. By contrast, using the ice-sheet endmembers with $\delta^{18}O$ values of −20‰ and −30‰ requires SSS changes of around 2–4 p.s.u. during Heinrich Stadials 1 and 4. Such SSS changes, and the observed magnitude of surface $\delta^{18}O_{sw}$ depletion of 2‰–3‰, are supported by our LGM_NA+NP experiment (Fig. 3h, i).

SSTs in the Equatorial Pacific and the Aleutian Low. Tropical SST responses are generally used to explain the enhanced Aleutian Low during North Atlantic cold events[27]. As a consequence of warming in the eastern Equatorial Pacific, rainfall in the western Pacific decreased by weakening the Walker Circulation and strengthening the Aleutian Low through triggering the Pacific–North American pattern[27]. To substantiate this dynamic link in our study, and to evaluate the different regional contributions of climatological SST changes to climate responses over the North Pacific between the LGM and Heinrich Stadial 1, we conducted five sensitivity experiments in ECHAM5 (L19/T31), the atmospheric component of our GCM (AGCM) (Extended Data Table 1). In these AGCM experiments, we used LGM boundary conditions (that is, orbital parameters, topography land–sea mask, ice sheet and greenhouse-gas concentrations). The 'atmospheric LGM' (A_LGM) control run in the AGCM was forced by climatology monthly mean SSTs and sea-ice cover from the LGM control experiment of the fully coupled GCM COSMOS; the 'atmospheric Heinrich Stadial 1' (A_HS1) control run in the AGCM was forced by SSTs and sea-ice cover from the hosing experiment LGM_NA.

To investigate the individual contributions of SST changes over different basins to Aleutian Low development over the North Pacific during Heinrich Stadial 1, we conducted three sensitivity experiments in which regional SST fields from the experiment LGM_NA were imposed upon the LGM control SST background, such as the Atlantic basin (30° S to 80° N) (A_HS1_Atl), the eastern Equatorial Pacific (180° E to around 70° W, 25° S to 25° N) (A_HS1_EEP), and a combination of the Atlantic and eastern Equatorial Pacific (A_HS1_EEPAtl), similar to ref. [66]. The atmosphere model was integrated for 50 years for each model experiment, and the last 30 years were taken to calculate climatological fields. Through these AGCM runs, we quantified the contributions of SST changes in the Atlantic and/or Equatorial Pacific to the strength of the Aleutian Low (Extended Data Fig. 4c–f). It is evident that warming in the eastern Equatorial Pacific is crucial for strengthening of the Aleutian Low as the AMOC slows down. In addition, the simulated eastern Equatorial Pacific warming in our fully coupled AO-GCM COSMOS is broadly consistent with glacial North Atlantic hosing experiments of other Palaeoclimate Modelling Intercomparison Project 3 (PMIP3) models[2]. We therefore suggest that warming of the Equatorial Pacific is a key component that bridges North Atlantic cooling to northeastern North Pacific subsurface warming by modulating the strength of the Aleutian Low.

Background cooling and North Pacific subsurface temperature. Subsurface temperature in the northeastern North Pacific is subject to the combined effects of cold-water masses from the northwestern North Pacific and warm-water masses from the (sub)tropical North Pacific. Therefore, it is plausible that enhanced cooling in the northern high latitudes can weaken and even reverse the subsurface warming in the northern North Pacific that is associated with northward advection of (sub)tropical warm-water masses. This will eventually stabilize the marine-based CIS, reducing meltwater input from the CIS. The boundary conditions during Heinrich Stadial 3—resulting from the lower obliquity compared with Heinrich Stadials 1 and 4—appear to favour the enhanced cooling in the northern high latitudes, ameliorating the collapse of marine-based ice along the North Pacific coastlines. To test this hypothesis, we conducted a North Atlantic hosing experiment (0.15 Sv) under the boundary conditions of 30 kyr ago (30kyr_NA) to mimic the freshwater flux to the North Atlantic during Heinrich Stadial 3 (Extended Data Table 1). Given the uncertainties of sea-level reconstructions[67,68] and the similar greenhouse gases at 21 kyr and 30 kyr before present (ref. [69]), we specify the 30-kyr-ago orbital parameters[70] to our LGM experiment to represent the climate of 30 kyr ago. This also helps us to quantify the additional contribution of the low obliquity to the high-latitude cooling under LGM conditions. As shown in Fig. 3, the 30kyr_NA results substantiate our hypothesis that additional high-latitude cooling associated with low obliquity during Heinrich Stadial 3 causes the subsurface cooling in the northeastern North Pacific, reducing the retreat of the marine-based CIS.

It is worth noting that other factors (the strength of the AMOC itself, ice-sheet configurations, greenhouse gases, and so on) can also determine the background climate. In the above hosing experiments, the ice-sheet configuration and greenhouse gases are identical to their LGM levels, which already lead to a cold background climate. In this context, in addition to lowering the annual mean insolation by obliquity, reducing meridional heat transport by the AMOC should also be able to cool down the northern high latitudes further during Heinrich Stadials. This is corroborated by an extreme LGM North Atlantic hosing experiment (with 0.2 Sv freshwater input) in which the AMOC shuts down (LGM_NA02) (Extended Data Table 1 and Extended Data Fig. 5d–g). As expected, an overall cooling appears in the subsurface of the northern North Pacific, although the simulated Aleutian Low and tropical warming get even stronger.

CIS meltwater events and North Atlantic circulation. To qualify the impact of CIS meltwater events on North Atlantic circulation during Heinrich Stadial 1, we performed a North Pacific-alone hosing experiment (0.1 Sv) under LGM boundary conditions (LGM_NP) (Extended Data Table 1). The experiment was integrated for 600 model years, and the average of the last 100 years is used to represent the corresponding climatology. It appears that North Pacific-alone hosing leads to robust subsurface warming in the North Pacific (Extended Data Fig. 5b); this warming acts as a positive feedback to maintain and/or accelerate the retreat of marine-based CIS ice. Note that, for the North Pacific, the term 'subsurface' is used for water depths of 120–180 m, according to the glacial northeastern North Pacific shelf depth. The North Atlantic, on the other hand, is characterized by discernible subsurface cooling (below around 100 m) (Extended Data Fig. 5c). Assuming that Heinrich events are related to subsurface warming (at roughly 100–1,200 m) in the North Atlantic[28,71,72], subsurface cooling would rather hamper the occurrences of Heinrich events by stabilizing the marine-based ice in the North Atlantic region. Therefore, it is more likely that changes in the North Atlantic are triggering North Pacific ice-rafting events during Heinrich Stadials than vice versa.

Code availability. The standard model code of the Community Earth System Models (COSMOS) version COSMOS-landveg r2413 (2009) is available upon request from the Max Planck Institute for Meteorology in Hamburg (https://www.mpimet.mpg.de). The code for the BACON software used for age-model construction can be obtained from http://www.chrono.qub.ac.uk/blaauw/.

Data availability. Our data can be obtained from the PANGAEA database at https://pangaea.de (https://doi.org/10.1594/PANGAEA.887506) and/or can be found in the Extended Data. No statistical methods were used to predetermine sample size.

31. Ruth, U. et al. Ice core evidence for a very tight link between North Atlantic and east Asian glacial climate. *Geophys. Res. Lett.* **34**, L03706 (2007).
32. Serno, S. et al. Comparing dust flux records from the Subarctic North Pacific and Greenland: implications for atmospheric transport to Greenland and for application of dust as a chronostratigraphic tool. *Paleoceanography* **30**, 583–600 (2015).
33. Hendy, I. L., Kennett, J. P., Roark, E. B. & Ingram, B. L. Apparent synchroneity of submillennial scale climate events between Greenland and Santa Barbara Basin, California from 30-10 ka. *Quat. Sci. Rev*. **21**, 1167–1184 (2002).
34. Cartapanis, O., Tachikawa, K. & Bard, E. Northeastern Pacific oxygen minimum zone variability over the past 70 kyr: impact of biological production and oceanic ventilation. *Paleoceanography* **26**, PA4208 (2011).
35. Blaauw, M. & Christen, A. J. Flexible paleoclimate age-depth models using an autoregressive gamma process. *Bayesian Anal*. **6**, 457–474 (2011).
36. Reimer, P. J. et al. INTCAL13 and MARINE13 radiocarbon age calibration curves 0-50,000 years cal BP. *Radiocarbon* **55**, 1869–1887 (2013).
37. Sarnthein, M., Balmer, S., Grootes, P. M. & Muddelsee, M. Planktic and benthic ^{14}C reservoir ages for three ocean basins calibrated by a suite of ^{14}C plateaus in the glacial-to-deglacial Suigetsu atmospheric ^{14}C record. *Radiocarbon* **57**, 129–151 (2015).
38. Maier, E. et al. Combined oxygen and silicon isotope analysis of diatom silica from a deglacial subarctic Pacific record. *J. Quat. Sci*. **28**, 571–581 (2013).
39. Sancetta, C. Distribution of diatom species in surface sediments of the Bering and Okhotsk seas. *Micropaleontology* **28**, 221–257 (1982).
40. Sancetta, C. Three species of *Coscinodiscus* Ehrenberg from North Pacific sediments examined in the light and scanning electron microscopes. *Micropaleontology* **33**, 230–241 (1987).
41. Swann, G. E. A. & Leng, M. J. A review of diatom $\delta^{18}O$ in palaeoceanography. *Quat. Sci. Rev*. **28**, 384–398 (2009).
42. Taylor, H. P. J. The oxygen isotope geochemistry of igneous rocks. *Contrib. Mineral. Petrol*. **19**, 1–71 (1968).
43. Sheppard, A. M. F. & Gilg, H. A. Stable isotope geochemistry of clay minerals. *Clay Miner*. **31**, 1–24 (1996).
44. Chapligin, B. et al. A high-performance, safer and semi-automated approach for the analysis of diatom silica and new methods for removing exchangeable oxygen. *Rapid Commun. Mass Spectrom*. **24**, 2655–2664 (2010).
45. Chapligin, B. et al. Inter-laboratory comparison of oxygen isotope compositions from biogenic silica. *Geochim. Cosmochim. Acta* **75**, 7242–7256 (2011).
46. Von Huene, R., Larson, E. & Crouch, J. in *Initial Reports of the Deep Sea Drilling Project*, Vol. XVIII (eds Musich, L. F. & Weser, O. E.) 835–842 (US Gov. Printing Office, Washington DC, 1973).
47. St John, K. E. K. & Krissek, L. A. Regional patterns of Pleistocene ice-rafted debris flux in the North Pacific. *Paleoceanography* **14**, 653–662 (1999).
48. Méheust, M., Fahl, K. & Stein, R. Variability in modern sea surface temperature, sea ice and terrigenous input in the sub-polar North Pacific and Bering Sea: reconstruction from biomarker data. *Org. Geochem*. **57**, 54–64 (2013).
49. Sikes, E. L., Volkman, J. K., Robertson, L. G. & Pichon, J.-J. Alkenones and alkenes in surface waters and sediments of the Southern Ocean: implications for paleotemperature estimation in polar regions. *Geochim. Cosmochim. Acta* **61**, 1495–1505 (1997).
50. Leclerc, A. J. & Labeyrie, L. Temperature dependence of the oxygen isotopic fractionation between diatom silica and water. *Earth Planet. Sci. Lett*. **84**, 69–74 (1987).
51. Waelbroeck, C. et al. Sea-level and deep water temperature changes derived from benthic foraminifera isotopic records. *Quat. Sci. Rev*. **21**, 295–305 (2002).
52. Takahashi, K. Seasonal fluxes of pelagic diatoms in the subarctic Pacific, 1982–1983. *Deep-Sea Res*. **33**, 1225–1251 (1986).
53. Epstein, S. & Sharp, R. P. Oxygen-isotope variations in the Malaspina and Saskatchewan glaciers. *J. Geol*. **67**, 88–102 (1959).
54. Dansgaard, W. & Tauber, H. Glacier oxygen-18 content and Pleistocene ocean temperatures. *Science* **166**, 499–502 (1969).
55. IAEA/WMO. Global Network of Isotopes in Precipitation. *The GNIP Database* http://www.iaea.org/water (2015).
56. Jakobsson, M. et al. Post-glacial flooding of the Bering Land Bridge dated to 11calka BP based on new geophysical and sediment records. *Clim. Past* **13**, 991–1005 (2017).
57. Roeckner, E. et al. *The Atmospheric General Circulation Model ECHAM5. Part 1: Model Description* (Max Planck Inst. Meteorol. Rep. 349, 2003).
58. Brovkin, V., Raddatz, T., Reick, C. H., Claussen, M. & Gaylor, V. Global biogeophysical interactions between forest and climate. *Geophys. Res. Lett.* **36**, L07405 (2009).
59. Marsland, S. J., Haak, H., Jungclaus, J. H., Latif, M. & Röske, F. The Max-Planck-Institute global ocean/sea ice model with orthogonal curvilinear coordinates. *Ocean Model*. **5**, 91–127 (2003).
60. Hibler, W. III A dynamic thermodynamic sea ice model. *J. Phys. Oceanogr*. **9**, 815–846 (1979).
61. Zhang, X., Lohmann, G., Knorr, G. & Purcell, C. Abrupt glacial climate shifts controlled by ice sheet changes. *Nature* **512**, 290–294 (2014).
62. Zhang, X., Knorr, G., Lohmann, G. & Barker, S. Abrupt North Atlantic circulation changes in response to gradual CO_2 forcing in a glacial climate state. *Nat. Geosci*. **10**, 518–523 (2017).
63. Monterey, G. & Levitus, S. *Seasonal Variability of Mixed Layer Depth for the World Ocean* (NOAA Atlas NESDIS 14, US Gov. Printing Office, Washington DC, 1997).
64. Kuroyanagi, A., Kawahata, H. & Nishi, H. Seasonal variation in the oxygen isotopic composition of different-sized planktonic foraminifer Neogloboquadrina pachyderma (sinistral) in the northwestern North Pacific and implications for reconstruction of the paleoenvironment. *Paleoceanography* **26**, PA4215 (2011).
65. Mulitza, S. et al. Temperature: $\delta^{18}O$ relationships of planktonic foraminifera collected from surface waters. *Palaeogeogr. Palaeoclimatol. Palaeoecol*. **202**, 143–152 (2003).
66. Zhang, Y. et al. Equatorial Pacific forcing of western Amazonian precipitation during Heinrich Stadial 1. *Sci. Rep*. **6**, 35866 (2016).
67. Lambeck, K. & Chappell, J. Sea level change through the last glacial cycle. *Science* **292**, 679–686 (2001).
68. Grant, K. M. et al. Rapid cooling between ice volume and polar temperature over the past 150,000 years. *Nature* **491**, 744–747 (2012).
69. Köhler, P., Nehrbass-Ahles, C., Schmitt, J., Stocker, T. F. & Fischer, H. A. 156 kyr smoothed history of the atmospheric greenhouse gases CO_2, CH_4, and N_2O and their radiative forcing. *Earth Syst. Sci. Data* **9**, 363–387 (2017).
70. Berger, A. L. Long-term variations of caloric insolation resulting from the Earth's orbital elements. *Quat. Res*. **9**, 139–167 (1978).
71. Flückinger, J., Knutti, R. & White, J. W. C. Oceanic processes as potential trigger and amplifying mechanisms for Heinrich events. *Paleoceanography* **21**, PA2014 (2006).
72. Álvarez-Solas, J. et al. Heinrich event 1: an example of dynamic ice-sheet reaction to oceanic changes. *Clim. Past* **7**, 1297–1306 (2011).
73. Bronk Ramsey, C. et al. A complete terrestrial radiocarbon record for 11.2 to 52.8 kyr B.P. *Science* **338**, 370–374 (2012).
74. Gersonde, R. Documentation of sediment core SO202-27-6 (2010).
75. Laskar, J. et al. A long-term numerical solution for the insolation quantities of the Earth. *Astron. Astrophys*. **428**, 261–285 (2004).
76. Clague, J. J. & James, T. S. History and isostatic effects of the last ice sheet in southern British Columbia. *Quat. Sci. Rev*. **21**, 71–87 (2002).
77. Kaufman, D. S., Young, N. E., Briner, J. P. & Manley, W. F. Alaska palaeo-glacier atlas (version 2). *Dev. Quat. Sci*. **15**, 427–445 (2011).
78. Ehlers, J. & Gibbard, P. L. The extent and chronology of Cenozoic global glaciation. *Quat. Int*. **164-165**, 6–20 (2007).
79. Schlitzer, R. *Ocean Data View* https://odv.awi.de (2018).

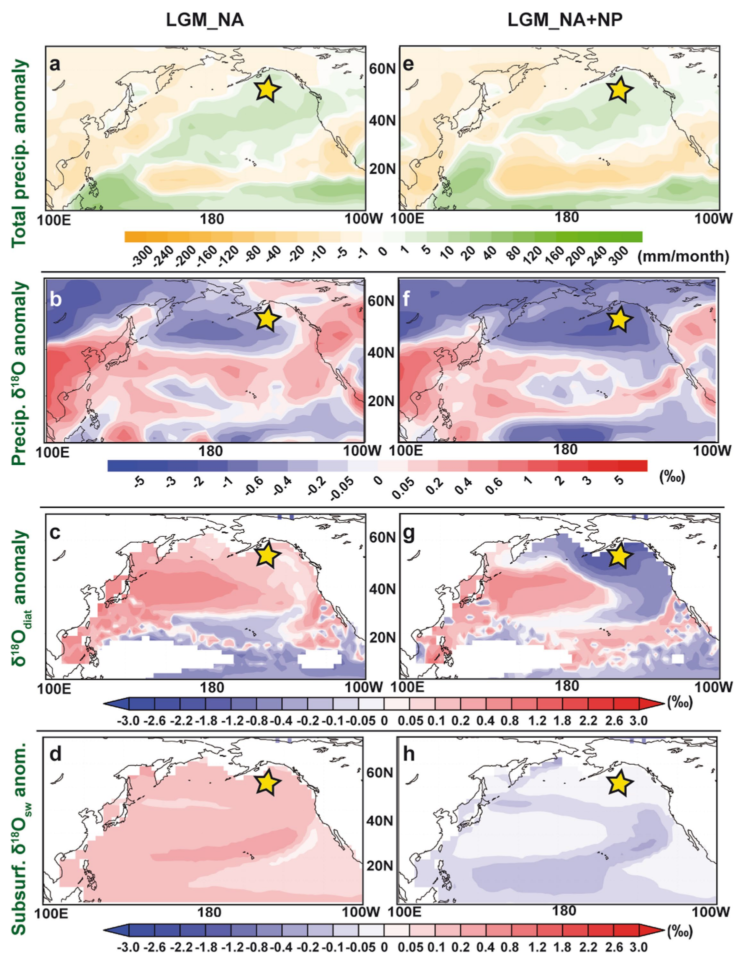

Extended Data Fig. 1 | Results from two freshwater hosing experiments. Left, LGM_NA; right LGM_NA+NP. Model results are presented as anomalies between the hosing simulations and the LGM state (see Methods). **a**, **e**, Total precipitation anomalies. **b**, **f**, Precipitation $\delta^{18}O$ anomalies. **c**, **g**, $\delta^{18}O_{diat.}$ anomalies. **d**, **h**, Subsurface $\delta^{18}O_{sw}$ anomalies (at depths of 120–180 m). The yellow star marks the location of core SO202-27-6.

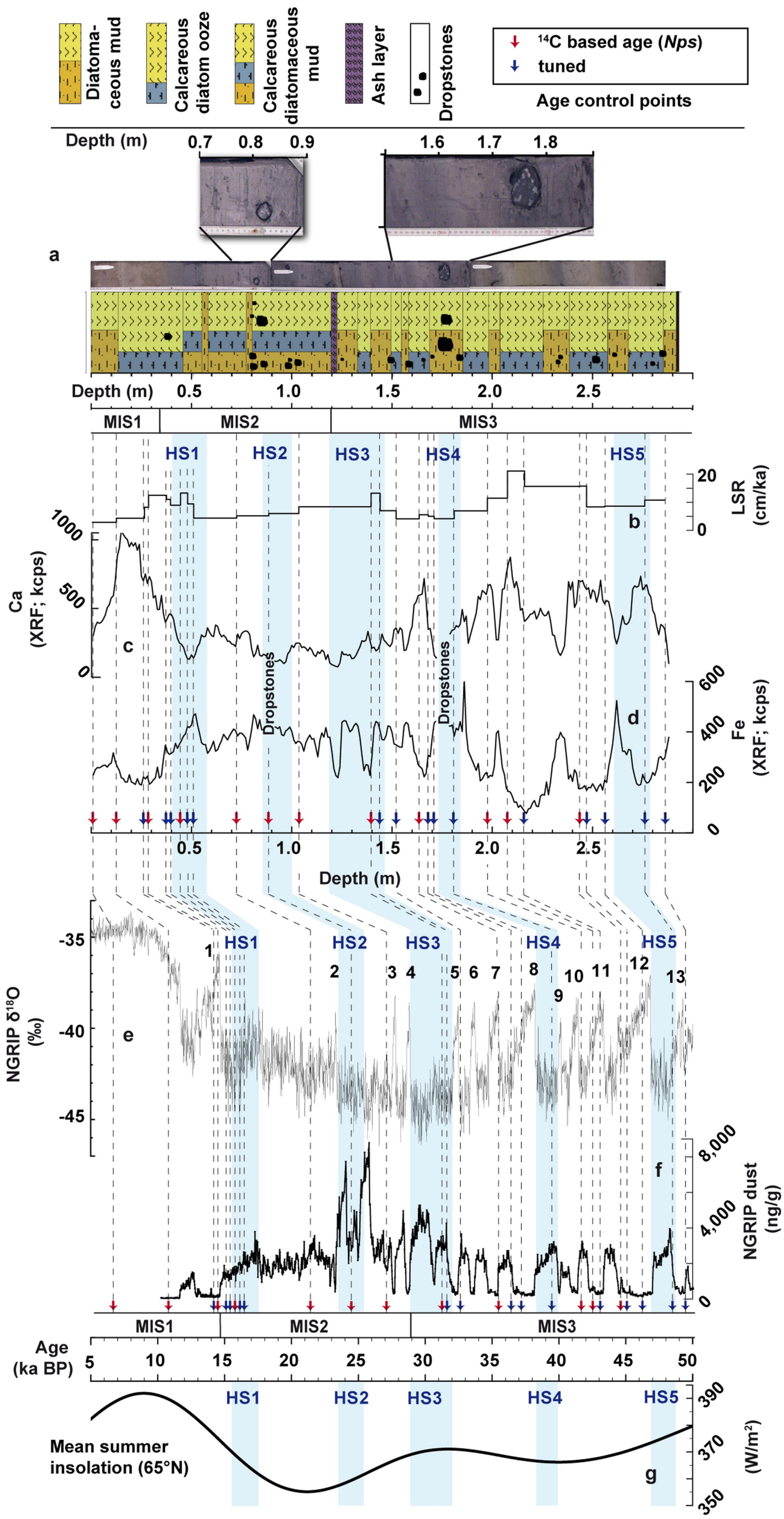

Extended Data Fig. 2 | Link between our data from core SO202-27-6, and NGRIP climate variabilities. **a–d**, SO202-27-6. **a**, Scheme and pictures describing the sediment core[74]. **b**, Linear sedimentation rate (LSR). **c**, Calcium intensity based on XRF analysis. **d**, Iron intensity based on XRF analysis. ka, thousands of years ago; kcps, thousands of counts per second. **e**, NGRIP $\delta^{18}O$ record[7]. **f**, NGRIP dust concentration[31], including age-control points for SO202-27-6. **g**, Mean summer insolation at 65° N (ref. [75]).

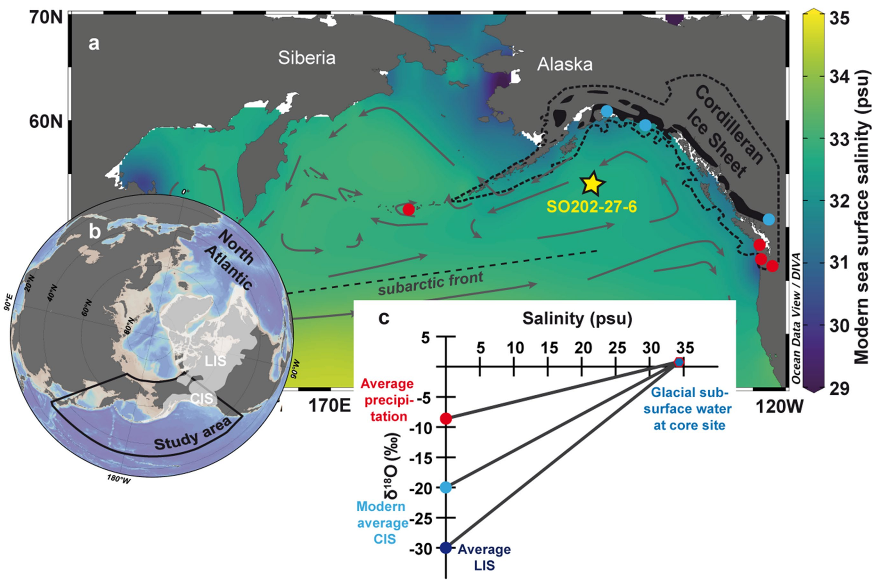

Extended Data Fig. 3 | SSS/$\delta^{18}O_{sw}$ mixing model for the last glacial open northeastern North Pacific. a, Study area as shown in Fig. 1, including the modern extent of the CIS (black), the extent of the CIS during the LGM[76,77] (black dashed line), the site of the studied core (yellow star), and the locations where precipitation (red dots) and modern glacier (light blue dots) parameters were taken for the SSS/$\delta^{18}O_{sw}$ mixing model. **b**, Study area from the North Pacific. Shaded white areas represent the extents of the LIS and CIS during the LGM[78]. **c**, SSS/$\delta^{18}O_{sw}$ mixing model assuming linear regression between SSS and $\delta^{18}O_{sw}$. We used three low-salinity endmembers and one high-salinity endmember to estimate SSS changes at our core site between 43 kyr and 11 kyr ago (see Methods). The Northern Hemisphere map and the SSS map were created using Ocean Data View[79].

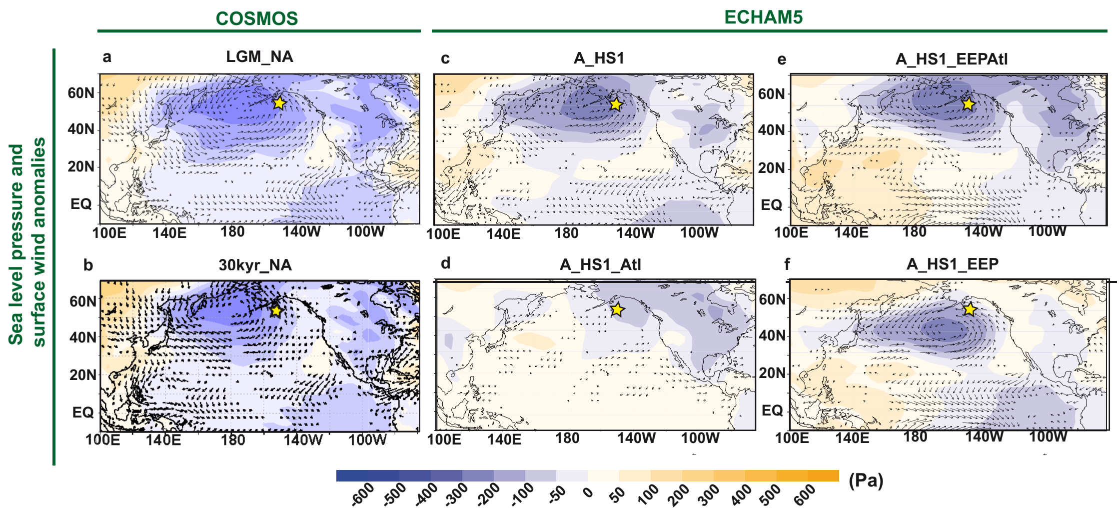

Extended Data Fig. 4 | Sea-level-pressure and surface-wind anomalies in our hosing experiments. a, **b**, Results obtained using COSMOS. **a**, LGM_NA experiment. **b**, 30kyr_NA experiment. **c–f**, Results obtained using ECHAM5. **c**, A_HS1 experiment. **d–f**, A_HS1 experiment, imposing SST fields on the Atlantic Basin (Atl) only (**d**), the Atlantic Basin and the east Equatorial Pacific (EEP; **e**), and the EEP only (**f**). The yellow star marks the location of studied Core SO202-27-6. Surface-wind anomalies (vectors) are presented in m s^{-1}. Sea-level-pressure anomalies are shown with shading.

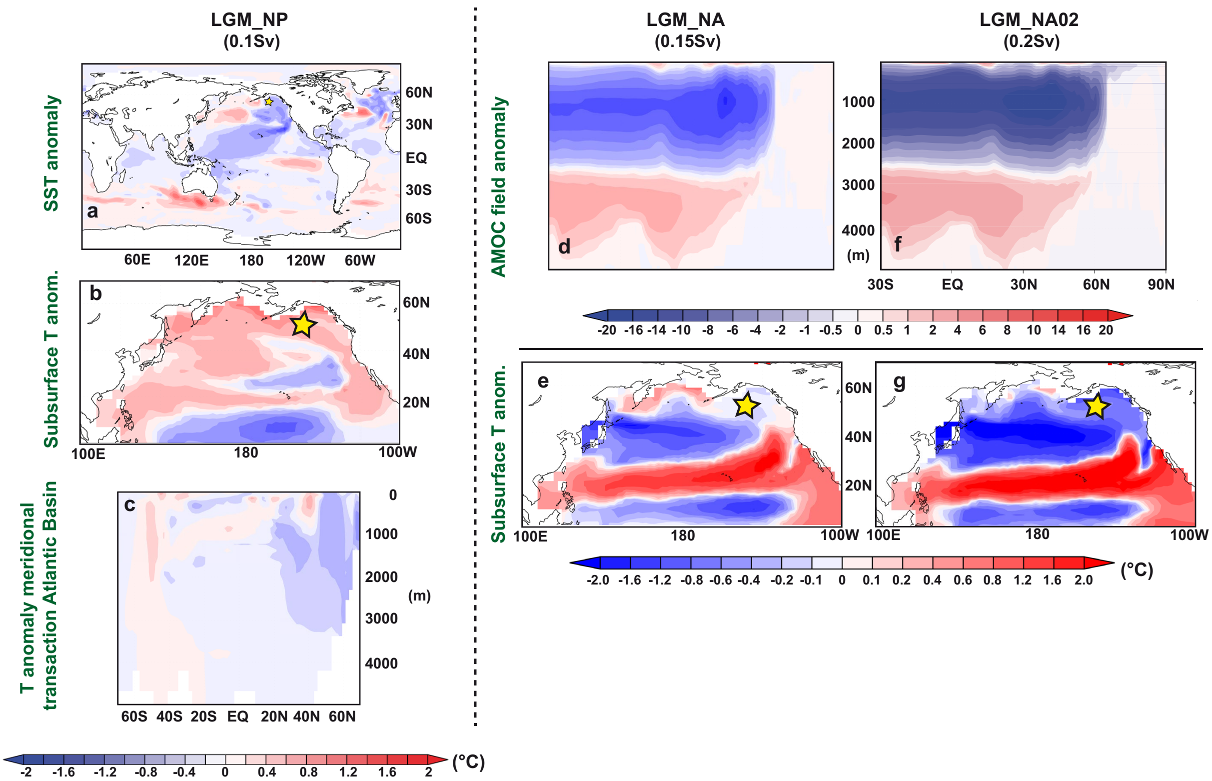

Extended Data Fig. 5 | Results from freshwater hosing experiments LGM_NP, LGM_NA and LGM_NA02, presented as anomalies. **a–c**, LGM_NP experiment (0.1 Sv). **a**, Global SST anomaly; **b**, North Pacific subsurface temperature anomaly (120–180 m). **c**, Temperature anomaly over the meridional transaction of the Atlantic basin (60° W to 15° W). **d–g**, LGM_NA experiment (0.15 Sv) (**d**, **e**) and LGM_NA02 experiment (0.2 Sv) (**f**, **g**). **d**, **f**, AMOC field anomalies. **e**, **g**, Subsurface temperature anomalies (120–180 m). The yellow star marks the location of core SO202-27-6.

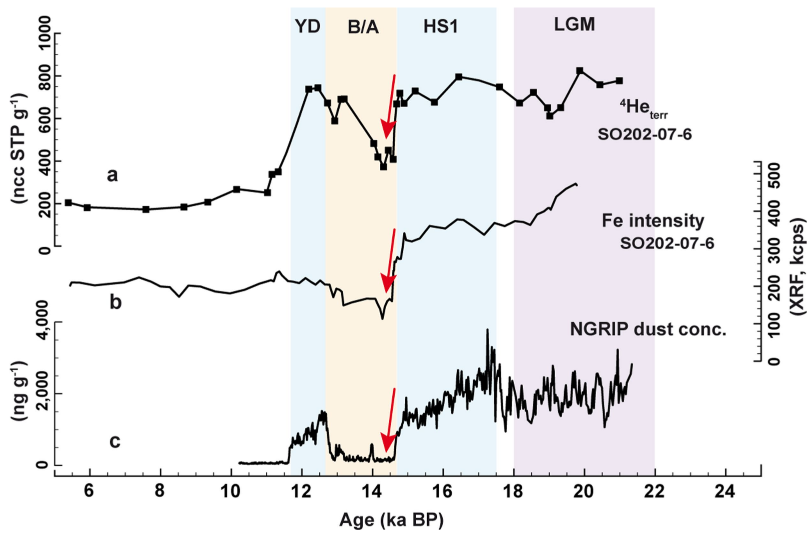

Extended Data Fig. 6 | Comparison of northwestern North Pacific eolian dust and iron intensity, as well as NGRIP dust concentration over the last deglaciation. a, Eolian dust (terrestrial ^{4}He concentration)[32] and **b**, iron intensity from core SO202-07-6 (51.3° N, 167.7° E; 2,340 m water depth). **c**, NGRIP dust concentration[31]. Dust changes in the northwestern North Pacific and Greenland are synchronous[32], and coincide with iron-intensity changes in the northwestern North Pacific. B/A, Bølling/Allerød interstadial; YD, Younger Dryas cold period. Red arrows mark chronological coincidence between the changes in ^{4}He, iron intensity and NGRIP dust concentration; ncc STP g^{-1}, nano-cubic centimetre per gram at standard temperature and pressure.

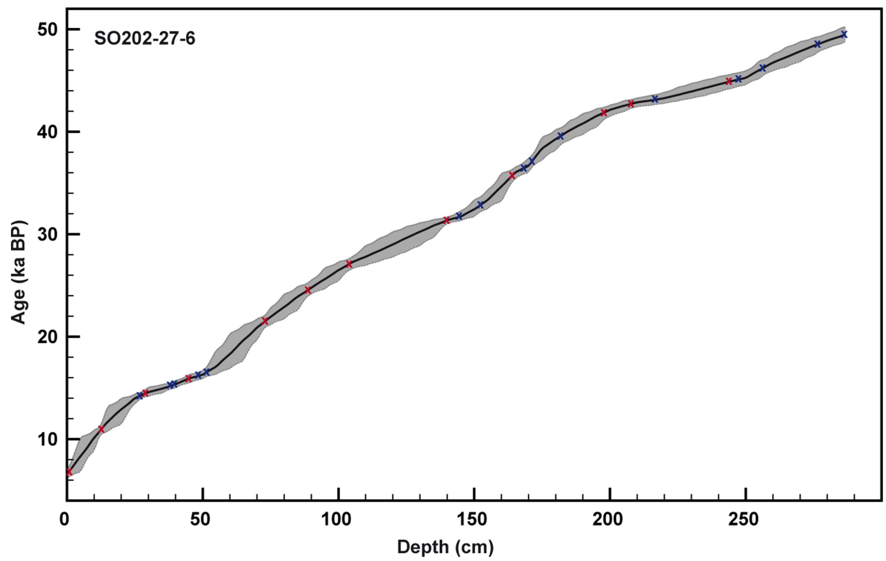

Extended Data Fig. 7 | Age–depth relationship for core SO202-27-6. The grey envelope shows the 95% confidence interval around the median age (black line). Crosses indicate age-control points obtained from radiocarbon dating (red), and from proxy correlation to core MD02-2489 (ref. [12]) and the NGRIP dust record[31] (blue).

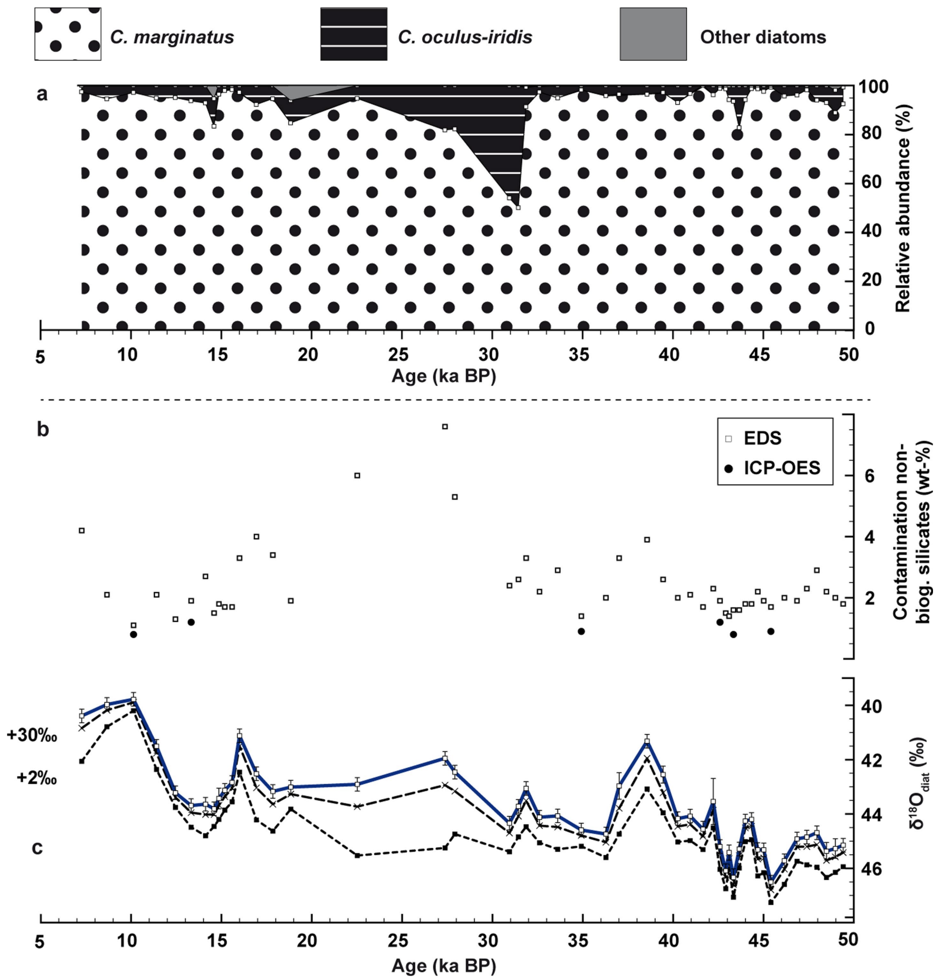

Extended Data Fig. 8 | Diatom isotope sample composition, residual contamination with non-biogenic silicates and mass-balance-corrected $\delta^{18}O_{diat.}$ (from core SO202-27-6). **a**, Relative abundances of the following diatom species in the isotope samples: *C. marginatus*, *C. oculus-iridis*, and other diatom species. **b**, Contamination of purified diatom samples with non-biogenic silicates, estimated by inductively coupled plasma optical emission spectrometry (ICP-OES) and energy-dispersive X-ray spectrometry (EDS). **c**, Blue line, measured $\delta^{18}O_{diat.}$ values (error bars indicate errors of replicate analyses or long-term reproducibility of standards (1σ)). Black dotted lines, $\delta^{18}O_{diat.}$ values that have been mass-balance-corrected for contamination with non-biogenic silicates (estimated by EDS), and using one of two different $\delta^{18}O$ values for non-biogenic silicate contamination (+2‰ or +30‰). Contamination values, $\delta^{18}O_{diat.}$ values and mass-balance-corrected $\delta^{18}O_{diat.}$ values younger than 25 kyr BP are taken from ref. [12].

Extended Data Table 1 | Overview of model experiments

a

COSMOS Experiment	Boundary conditions	Orbital parameters	FWF amount	FWF IsoV	Integrated years
LGMctl	21 ka	21 ka	-	-	5000
LGM_NA	21 ka	21 ka	0.15 Sv NA	30‰	800
LGM_NA+NP	21 ka	21 ka	0.15 Sv NA + 0.1 Sv NP	30‰	800
LGM_NA02	21 ka	21 ka	0.2 Sv NA	30‰	800
LGM_NP	21 ka	21 ka	0.1 Sv NP	30‰	600
30kyr_ctl	21 ka	30 ka	-	-	800
30kyr_NA	21 ka	30 ka	0.15 Sv NA	30‰	600

b

ECHAM5 Experiment	Boundary conditions	SST forcing
A_LGM	21 ka	LGMctl global SST
A_HS1	21 ka	LGM_NA global SST
A_HS1_Atl	21 ka	LGMctl SST background, but with LGM_NA SST only in the Atlantic
A_HS1_EEPAtl	21 ka	LGMctl SST background, but with LGM_NA SST in the Atlantic and EEP
A_HS1_EEP	21 ka	LGMctl SST background, but with LGM_NA SST only in the EEP

a, Experiments conducted with the fully coupled GCM COSMOS. The boundary conditions include ice-sheet configuration, land–sea mask (land mask that is related to the sea-level changes in the past), glacial extent, greenhouse gases, etc., except the orbital parameters (see Methods). FWF, freshwater forcing; IsoV, isotopic values; NA, North Atlantic (40–55° N, 20–45° W); NP, North Pacific (50–60° N, 143–172° W); 1 Sv $= 10^6$ m^3 s^{-1}. 'Years' here refers to model years.
b, Experiments conducted with ECHAM5 (the atmospheric component of COSMOS).

Extended Data Table 2 | Age constraints of core SO202-27-6

Sample ID/ Age control point	Depth (cm)	^{14}C ages (ka)	^{14}C age error (a)	Reservoir age (Delta-R) (a)	Reservoir age error (1σ) (a)	Lake Suigetsu varve error (1σ) (a)	NGRIP tuning error (1σ) (a)	Median ages (ka BP)
OS-85661	0.5	6.090	30	40	173	-	-	**6.713**
OS-85752	12.5	9.880	30	40	173	-	-	**10.923**
LS-1	26.5	-	-	-	-	102	-	**14.173**
OS-87903	28.5	13.050	55	40	173	108	-	**14.415**
LS-2	37.5	-	-	-	-	132	-	**15.137**
LS-3	39.5	-	-	-	-	148	-	**15.318**
OS-85753	44.5	13.900	30	150	185	165	-	**15.876**
LS-4	48.0	-	-	-	-	179	-	**16.140**
LS-5	51.0	-	-	-	-	190	-	**16.459**
OS-87888	72.5	18.750	70	710	202	-	-	**21.401**
OS-87894	88.5	21.400	120	710	202	-	-	**24.500**
OS-87892	103.5	23.800	110	710	202	-	-	**27.022**
OS-88043	139.5	28.300	140	710	202	-	-	**31.303**
NG-1	144.0	-	-	-	-	-	375	**31.643**
NG-2	152.0	-	-	-	-	-	375	**32.792**
OS-87893	163.5	33.000	170	710	202	-	-	**35.594**
NG-3	168.0	-	-	-	-	-	375	**36.410**
NG-4	171.0	-	-	-	-	-	375	**37.013**
NG-5	181.0	-	-	-	-	-	375	**39.441**
OS-87899	197.5	38.400	310	710	202	-	-	**41.823**
OS-87889	207.5	39.900	290	710	202	-	-	**42.694**
NG-6	216.0	-	-	-	-	-	375	**43.096**
OS-87898	243.5	42.800	600	710	202	-	-	**44.854**
NG-7	247.0	-	-	-	-	-	375	**45.076**
NG-8	256.0	-	-	-	-	-	375	**46.158**
NG-9	276.0	-	-	-	-	-	375	**48.485**
NG-10	286.0	-	-	-	-	-	375	**49.413**

Apart from planktic (sinistral *N. pachyderma*) ^{14}C ages, additional age-control points were obtained through correlation to the high-resolution Lake Suigetsu record—via proxy correlation to core MD02-2489 (ref. [12])—and through proxy correlation to the NGRIP dust record (see Methods). Radiocarbon ages and radiocarbon-age errors from the upper 90 cm are taken from ref. [12]. Reservoir ages and reservoir-age errors were assigned from nearby core MD02-2489 (ref. [37]). Lake Suigetsu varve errors are taken from ref. [73]. a, years ago.